Experiments on sound reflection and production by choked nozzle flows subject to acoustic and entropy waves

Journal of Sound and Vibration xxx (xxxx) xxx

Contents lists available at ScienceDirect

Journal of Sound and Vibration

journal homepage: www.elsevier.com/locate/jsv

Special Issue: Recent Advances in Acoustic Black Hole Research

Experiments on sound reflection and production by choked nozzle flows subject to acoustic and entropy waves

Markus Weilenmann, Nicolas Noiray*

CAPS Laboratory, Department of Mechanical and Process Engineering, ETH Zurich, Zurich 8092, Switzerland

ARTICLE INFO

Article history:
Received 30 June 2020
Revised 26 September 2020
Accepted 16 October 2020
Available online xxx

Keywords:
Entropy waves
Indirect noise
Thermoacoustic instabilities
Choked nozzle flow

ABSTRACT

The acceleration of entropy waves in the turbine stages of aero-engines and gas turbines produces sound, which can contribute to the feedback mechanism of thermoacoustic instabilities. These instabilities cause high cycle fatigue of the combustor components, which may lead to catastrophic engine failure. This work deals with the challenging problem of experimentally quantifying entropy-wave-induced sound production from nozzles under choked flow conditions, at frequencies and turbulence intensities that are relevant for practical applications. There is a substantial need for such experimental data in order to validate predictive models of thermoacoustic instabilities involving entropy waves. In this study, the transfer function linking incident entropy waves, produced by a pulsed hot jet in a non-reactive turbulent cross flow, and the resulting reflected acoustic waves from choked nozzle flows are identified by combining acoustic measurements, background-oriented Schlieren thermometry and particle image velocimetry. The transfer function is measured for frequencies comprised between 60 and 180 Hz in the case of entropy waves that undergo intense dispersion in the highly turbulent channel, and that exhibit, at their arrival at the supercritical nozzle, amplitudes ranging from −1 to 10 percent of the mean temperature. This work suggests that three-dimensional deformation of entropy spots upstream of the nozzle convergent is likely to play a key role in the sound generation process, and can be used for developing new models accounting for this phenomenon.

1. Introduction

The entropy waves within the focus of this study are essentially temperature fluctuations, which result from the unsteadiness of the combustion process and the mixing of burned gases with dilution air. They are advected toward the turbine of aero engines and gas turbines. Their acceleration in the turbine vanes leads to the production of sound, which is radiated in both upstream and downstream directions [1]. Sound can also be produced by the acceleration of compositional [2] or vortical disturbances [3]. For the design of modern combustion technologies, these sound sources are an increasingly important issue due to the following two reasons.

First, the broadband component of these sound sources significantly contributes to the overall noise emission of aero engines and therefore of aircrafts. It is referred to as *indirect combustion noise* [4–6] as opposed to the *direct combustion*

* Corresponding authors.
E-mail addresses: wemarkus@ethz.ch (M. Weilenmann), noirayn@ethz.ch (N. Noiray).

https://doi.org/10.1016/j.jsv.2020.115799

noise resulting from the unsteadiness of the flame's heat release rate, because the temperature, compositional and vortical disturbances at the turbine inlet are by-products of the unsteady combustion process. With more stringent noise pollution regulations, this is an important aspect which must be accounted for in the design of future combustors.

Second, modern combustors, which are operated under leaner regimes for decreasing pollutant emissions, are more prone to thermoacoustic instabilities [7], which can involve entropy-wave-induced acoustic waves in their feedback loop [8]. These instabilities induce strong mechanical vibration that can ultimately lead to the destruction of the engine. Therefore, for ensuring safe and reliable operation, it is crucial to keep thermoacoustic instabilities under control, which necessitates the development of predictive models of their potential underlying mechanisms, including the entropy wave feedback.

Regarding the latter mechanism, three main processes have to be understood and modelled: 1) The production of entropy waves by an acoustically modulated combustion process, 2) the decay of entropy waves during their advection, 3) the conversion of entropy waves to sound during their acceleration at the combustor exit. This study focuses on the third process, which will be reviewed in detail after a brief digression about the recent progress in the other two areas.

Concerning the production of entropy waves in combustors, the acoustically-induced modulation of equivalence ratio has been identified as one of the main sources of entropy waves [9,10]. Very recently, it was shown experimentally that an array of technically-premixed turbulent jet flames generates significantly stronger entropy waves than a single turbulent swirled flame of the same thermal power and equivalence ratio [11]. The reason for this difference was attributed to the enhanced mixing induced by the swirling flow, which corroborate the findings in [10,12], where entropy waves originating from a turbulent swirled flame exhibit a fast decay and do not significantly participate in the thermoacoustic dynamics of the combustor investigated in this particular work. In [13], it was also shown that perfectly premixed turbulent swirl flames can also produce significant entropy waves under acoustic forcing, due to the periodic engulfment of recirculation gases in the flame plume. Effort has also been committed to numerical studies to investigate the production of temperature fluctuations in real configurations [14]. Also, significant work has been invested into the development of low order models to improve predictive capabilities [15,16].

Regarding the decay of entropy waves along the combustion chamber, several numerical studies were recently performed in order to predict the strength of these waves at the turbine inlet. For instance, the incompressible DNS in [17] showed that thermal dissipation of coherent entropy waves is negligible in a fully developed turbulent channel flow, while shear dispersion governs the amplitude decay. However, when considering non-adiabatic walls in similar channel flows [18], it was shown that thermal diffusion cannot be neglected in all cases, which was confirmed recently in [19], where a low-order model was proposed to account for two dimensional entropy waves. Furthermore, the advection of compositional waves was also numerically investigated in [20]. Other recent numerical studies explored the decay of entropy waves in industrial configurations [21,22], and the different mechanisms contributing to the decay of the entropy wave amplitude was reviewed in [23], where the scarcity of experimental data is highlighted. Indeed, only a few experimental studies were carried out on this problem, mostly because of the challenge of measuring fast and low amplitude temperature fluctuations. In a combined numerical and experimental study, a low order model for the decay of entropy waves in a non-reacting fully-developed turbulent flow was proposed and validated [24]. In [25], it was shown that large coherent turbulent structures, which develop in practical configurations, significantly enhanced the decay rate of coherent entropy waves.

Now returning to the topic of the current work, which is the generation of sound by the acceleration of entropy waves. This phenomenon has been studied numerically, analytically and experimentally. In the1970ʹs, using an analytical approach, Marble & Candel developed a linear one dimensional (1D) model for entropy-wave induced sound generation in compact subsonic and supercritical nozzle flows [26] with an extension to a non-compact nozzle with linear velocity profile. Since then, the model has been refined by adding non-linear effects in subsonic [27] and supercritical nozzle flows [28], relaxing the compactness assumption [29–32] adding reverberation [33] and accounting for non-isentropic flow [34]. A few numerical works have been performed on realistic geometries, e.g. [35]. Recently, new models have been developed to account for two dimensional (2D) entropy waves [36,37], which is an important step considering the evidence presented in the current work.

Experimental studies on this topic are challenging to perform, because temperature fluctuation measurements in gas streams are difficult to achieve and the separation of direct and indirect sound components is not trivial. Therefore, setups have been designed specifically for the investigation of the sound contribution originating from accelerated entropy waves. Using the entropy wave generator of DLR, Bake et al. presented measurements of acoustic pressure fluctuations resulting from accelerated, synthetically generated entropy waves, using a heating grid, and compared it to numerical results [38]. An increasing sound amplitude was found with increasing source strength, with a focus on single waves. The data was used as reference in several numerical studies [39–42]. The entropy wave generator, which was set up at Cambridge, also relies on an electric heating grid and the separation of sound produced by direct and indirect mechanisms is achieved by taking advantage of the respective different propagation speeds and by using a long exhaust tube to avoid acoustic reflections during the time-window for measurement [34,43].

The experimental data presented in the current paper represents a step towards more realistic flows, because entropy waves are generated by a temperature controlled pulsed jet-in-crossflow, with a highly turbulent main flow upstream of the nozzle. The mass flow rates is set around 200 g/s with 3 bars absolute pressure upstream of the nozzle for all the experiments with entropy wave forcing, which were performed for choked nozzle. For several test with pure acoustic forcing described in Section 4.1, the mass flow rate was set to lower values and the nozzle flow was subsonic. The resulting entropy waves in this rig are highly three dimensional and therefore closer to the ones expected in real systems [14]. To achieve separation of the entropy-wave induced acoustic-wave reflected by the nozzle from the one associated with the reflection

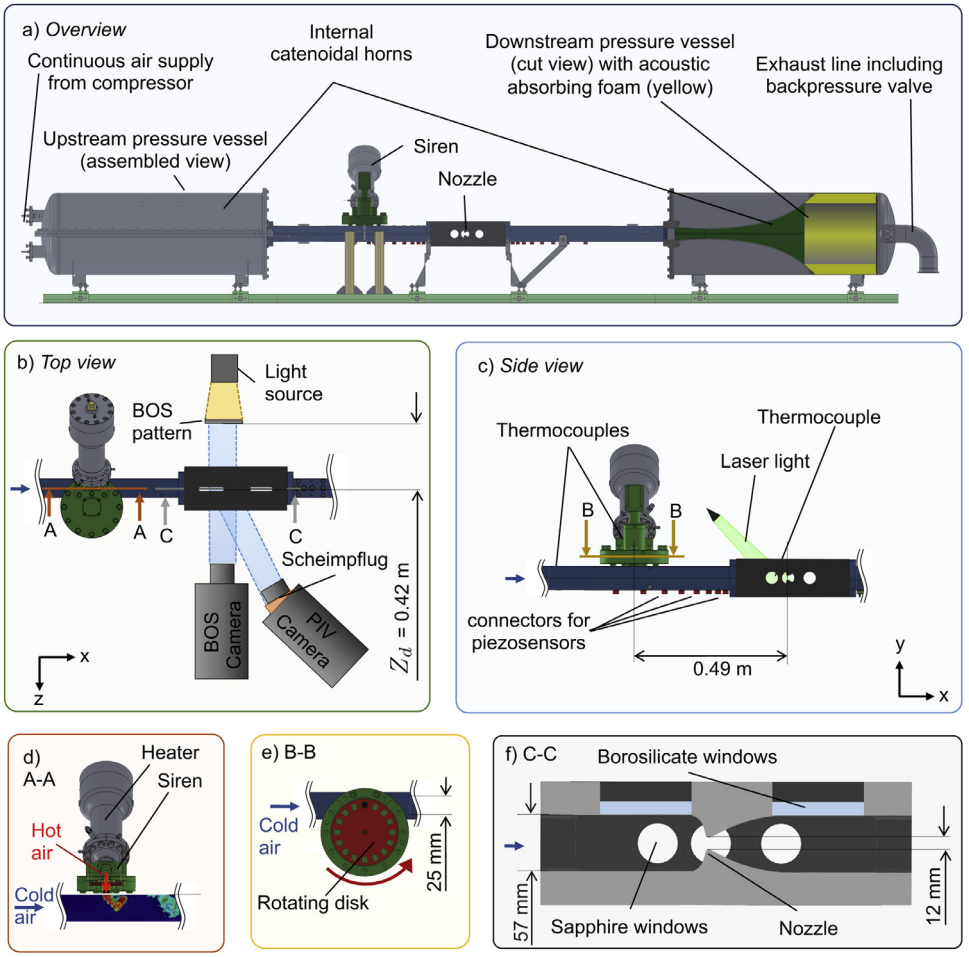

Fig. 1. a) Overview of the test rig, which is continuously supplied with a compressor. b) Test section and optical setup seen from the top. c) Side view of the test section. d) Vertical cut through the siren. e) Horizontal cut through the siren. f) Vertical cut through the nozzle section.

of the incident acoustic waves, the method proposed by Tao et al. [44], which was suffering from low signal-to-noise-ratio (SNR) in [44], is taken up in the present work, with a significantly increased SNR. The method is based on the comparison between acoustic reflection coefficients R of a sonic nozzle measured in the presence and absence of entropy waves for the same mean flow conditions. The advected, coherent, temperature fluctuation amplitude $\tilde{T}$, is measured using thermocouples and background-oriented Schlieren thermometry. By combining both methods, the contribution of entropy waves to the upstream sound field is quantified and compared to the compact 1D solution, which provides valuable data for the validation of models in harsh conditions.

2. Setup

The experimental setup, composed of a wind channel with rectangular cross-section, a siren capable of injecting a temperature-controlled pulsed jet-in-cross-flow and a nozzle, is shown in Fig. 1. The test rig was operated at static pressure differences across the nozzle, up to $\Delta p_n = 2$ bar, with a maximum inlet mass flow imposed upstream of the siren of $\dot{m}_{m,max} = 200$g/s. The experiments were conducted with a compressor continuously supplying this inlet airflow at thermal equilibrium, leading to a mean temperature of the flow $\bar{T}_m \approx 43^\circ$C. The mass flow and the pressure drop across the nozzle were adjusted with a precision pressure regulator,mass flow controller and a back pressure valve releasing the flow to the atmosphere, respectively placed between the compressor outlet plenum maintained at 5 bars (not shown) and the upstream pressure vessel. The back pressure valve was kept completely open (exit static pressure $\approx$ 950mbar) and the resulting mass flow was monitored using a mass flow meter, mounted upstream of the pressure regulator. Two transition pieces, of constant cross-section area, link the rectangular section channel to the two round section catenoidal horns placed in the pressure vessels. These horns and the 10 cm thick layer of acoustic foam that lines the two pressure vessels provide quasi-anechoic conditions for acoustic waves from the channel at frequencies above 500 Hz. The channel has constant in-

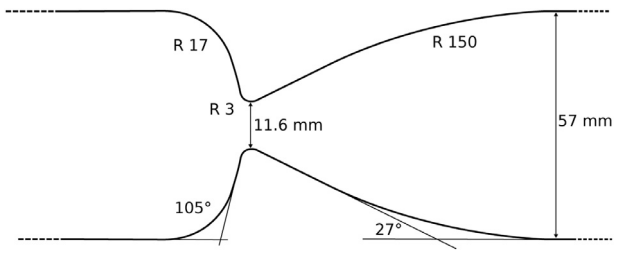

Fig. 2. Geometrical details of the nozzle used in this work. The radii of curvature are given in mm.

ner height and width, $H = 57$mm and $W = 25$mm respectively, with exception of the nozzle, where the height is reduced to $H_t = 12$mm at the nozzle throat (see Fig. 1(f)). The contour of the nozzle used in this work is shown in Fig. 2. In the proximity of the nozzle, optical access is possible from the top, through borosilicate windows and from the side through sapphire windows, as shown in Fig. 1(f). The optical diagnostics setup, also shown in Fig. 1(b), is explained in Section 3.2.

The siren consists of a rotating perforated disk and an electric heater supplied with pressurized air, at a constant rate of $\dot{m}_j = 15$g/s controlled by a precision pressure regulator and monitored by a mass flow meter, as shown in Fig. 1(d) and 1(e). The frequency of the pulsed jet-in-crossflow (diameter at injection 19 mm) is controlled by adjusting the rotation speed of the siren disk. The injected air pockets yield coherent entropy waves that are advected in the streamwise direction. For the reference measurements, it is preferable to set $\bar{T}_j = \bar{T}_m$, which was achieved by adjusting the heating power accordingly. To generate hot waves, the mean jet temperature $\bar{T}_j$ was chosen such that $\bar{T}_j > \bar{T}_m$. The copper supply pipe of the siren was guided through ice-water to allow the generation of colder than main flow waves ($\bar{T}_j < \bar{T}_m$) as well.

To measure the mean temperatures of the main flow $\bar{T}_m$, the jet air flow $\bar{T}_j$ and the mean temperature of the flow 5 cm upstream of the nozzle $\bar{T}_n$, thermocouples were placed at the locations indicated in Fig. 1(c). Differential static pressure probes were placed upstream and downstream of the test section and the ambient air pressure was noted during the experiments to determine the absolute pressure level inside the channel upstream and downstream of the nozzle. The acoustic pressure was recorded in the channel using 6 piezoelectric sensors of type 211B5 from Kistler.

3. Methodology

The local temperature in the channel is decomposed using the classic triple decomposition: $T(\boldsymbol{x},t) = \bar{T}(\boldsymbol{x}) + \tilde{T}(\boldsymbol{x},t) + \check{T}(\boldsymbol{x},t)$, where $\bar{T}$ is the mean temperature, $\tilde{T}$ and $\check{T}$ are the zero-mean coherent and turbulent components of the fluctuating temperature, $\langle T \rangle = \tilde{T} + \bar{T}$ the phase averaged temperature (taking the harmonic acoustic pressure for the phase reference), and $T' = \tilde{T} + \check{T}$ the zero-mean fluctuating temperature. The other variables are treated analogously. This study focuses on the coherent part of the temperature fluctuations $\tilde{T}(\boldsymbol{x},t)$ and the sound they produce when accelerated in the nozzle. Assuming small perturbations, the local zero-mean entropy fluctuations s' can be expressed as function of the temperature and pressure fluctuations, respectively T' and p'(see e.g. [6]). Since only the coherent component of the temperature fluctuations can be experimentally quantified in this work, this equation is phase-averaged and is written as:

$$\frac{\tilde{s}}{c_p} = \frac{\tilde{T}}{\bar{T}} - \frac{\gamma - 1}{\gamma}\frac{\tilde{p}}{\bar{p}}, \tag{1}$$

where c_p is the specific heat capacity and $\gamma = c_p/c_v$ the ratio of specific heats. For the conditions explored at the nozzle in this study, the normalised pressure fluctuations are small and the second term in Eq. (1) can be neglected compared to the first term. The entropy-waves-induced reflected acoustic waves are quantified using the approach explained in Section 3.1. The temperature waves $\tilde{T}(\boldsymbol{x},t)$ arriving at nozzle are measured using a combination of BOS and PIV, detailed in Section 3.2. It is worth mentioning that the entropy wave amplitude that is measured in this work just upstream of the nozzle, depends on the dispersion of the wave during its transport. In the present configuration, it was shown in [25] that the wave amplitude decreases by one order of magnitude for $St \simeq 3$, where the Strouhal number $St = \omega L/(2\pi \bar{u}_x)$ depends on the mean flow velocity $\bar{u}_x$, on the angular frequency ω and on the transport distance L of the entropy wave.

3.1. Acoustic measurements

A sketch of the test rig is presented in Fig. 3. The forward and backward acoustic waves resulting from the forcing of the loudspeaker (placed inside a pressure resistant casing) or of the siren are identified using the multi-microphone method [45]. The loudspeaker is used to produce a pure acoustic excitation upstream of the nozzle. When it is replaced by the siren, there is a net mean flow addition to the channel flow, and one can also impose a pure acoustic excitation in the channel, provided that the temperature of the pulsed jet $\bar{T}_j$ is set equal to the temperature of the main flow $\bar{T}_m$. However, when $\bar{T}_j \neq \bar{T}_m$, one generates a combination of acoustic and entropy waves. In such a situation, hot or cold temperature waves are advected towards the nozzle and their acceleration produces backward travelling acoustic waves, which accumulate to the reflection of incident acoustic waves.

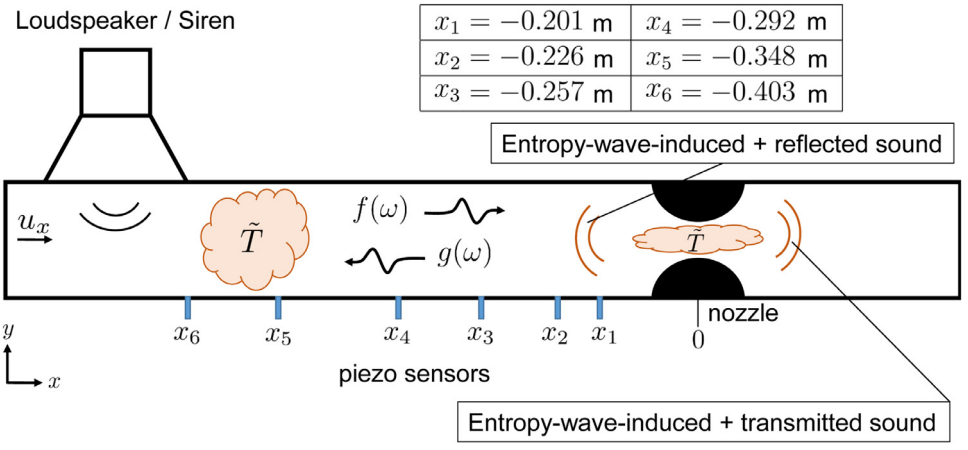

Fig. 3. Schematic of the experimental setup for measuring acoustic reflection coefficients. Acoustic wavelengths focused on in this work are comprised between 0.3 and 6 m: the acoustic reflection coefficient in absence of entropy waves was measured from 60 to 1000 Hz, and the entropy-wave-induced sound reflection was measured from 60 to 180 Hz.

The Fourier amplitude $\hat{p}(x,\omega)$ at the angular frequency ω of the forcing imposed by the loudspeaker or the siren is determined from the acoustic pressure signals recorded by 6 piezo sensors, placed as shown in Fig. 3. The acoustic pressure is expressed as the solution of the one-dimensional wave equation in a lossless waveguide with mean flow:

$$\frac{\hat{p}(x,\omega)}{\bar{\rho}\bar{c}} = f(\omega)e^{-i\frac{\omega}{\bar{c}}\frac{x}{1+\bar{M}}} + g(\omega)e^{i\frac{\omega}{\bar{c}}\frac{x}{1-\bar{M}}} \tag{2}$$

where the Riemann invariants $f(\omega)$ and $g(\omega)$ represent the complex amplitudes of the downstream and upstream propagating waves, travelling at velocities $\bar{c}+\bar{u}_x$ and $\bar{c}-\bar{u}_x$, with $\bar{c}$ being the speed of sound. The mean Mach number is denoted by $\bar{M} = \bar{u}_x/\bar{c}$. In several papers, e.g. [26,33,34], the following alternative classic notations for the Riemann invariants can be found: $P_1^+ = f/c$ and $P_1^- = g/c$, where the Riemann invariants are non-dimensional, while f and g used in the present study have units of velocity. Using all available piezo signals, the following system of equations is obtained:

$$\frac{1}{\bar{\rho}\bar{c}}\begin{bmatrix}\hat{p}_1\\ \vdots \\ \hat{p}_6\end{bmatrix} = \begin{bmatrix} z_1^{\frac{1}{1+\bar{M}}} & z_1^{\frac{-1}{1-\bar{M}}} \\ \vdots & \vdots \\ z_6^{\frac{1}{1+\bar{M}}} & z_6^{\frac{-1}{1-\bar{M}}}\end{bmatrix}\begin{bmatrix} f \\ g\end{bmatrix} \tag{3}$$

with $z_k = \exp(-i\omega x_k/\bar{c})$ and x_k being the axial position of piezo sensor k. The Riemann invariants f and g are solutions of the over-determined system in Eq. (3), obtained using least-square inversion [45]. The mean flow velocity $\bar{u}_x$ is determined from the sum of main and jet mass flow ($\dot{m}_{tot} = \dot{m}_m + \dot{m}_j$), measured using Bronkhorst mass flow meters, the cross section area of the channel ($25 \times 57 = 1425\text{mm}^2$), the mean flow temperature upstream of the nozzle $\bar{T}_n$ and the static pressure. It is worth noting that based on [46], the present spacing between the first and the last microphone ($L_m = x_1 - x_6 \simeq 0.2$ m) is adequate to measure acoustic reflection coefficients using the two-microphone method between 85 Hz and 680 Hz ($0.1\pi < \omega L_m/\bar{c} < 0.8\pi$). In this work, measurements were performed down to 60 Hz, which is below the lower limit given in [46]. However, here we use the multi-microphone method, which improves the measurement quality compared to the two-microphone method. Furthermore, it was checked that even below 85 Hz, the relative error between reconstructed and measured signals was below 5%.

The reflection coefficient of the nozzle is defined as the ratio of the reflected to the incident acoustic waves amplitude $R = g/f$. Since g results from the combination of incident-acoustic-wave reflection and entropy-wave induced acoustic wave, R can serve as a measure of sound production due to entropy wave acceleration in the nozzle. Indeed, the difference $\Delta R = R - R_{\text{ref}}$, where R_{ref} is the reference case at the same total mass flow but with $\bar{T}_m = \bar{T}_j$, can be attributed to the sound generated by the accelerated temperature waves $\tilde{T}(\boldsymbol{x},t)$, as undertaken in [44]. This approach is successfully employed in the present study for the reflected acoustic waves. However, for the considered range of entropy waves amplitudes, it was not possible to use it for evaluating the indirect combustion noise downstream of the nozzle, i.e. the entropy-wave-induced transmitted acoustic waves. This is because the shock in the nozzle produces very intense background noise and consequently a poor SNR.

3.2. BOS thermometry

BOS thermometry is achieved using a new methodology proposed in [25]. This method is based on a panoramic stitching of the displacement fields, which is briefly explained in the following paragraph, and which requires measurement of

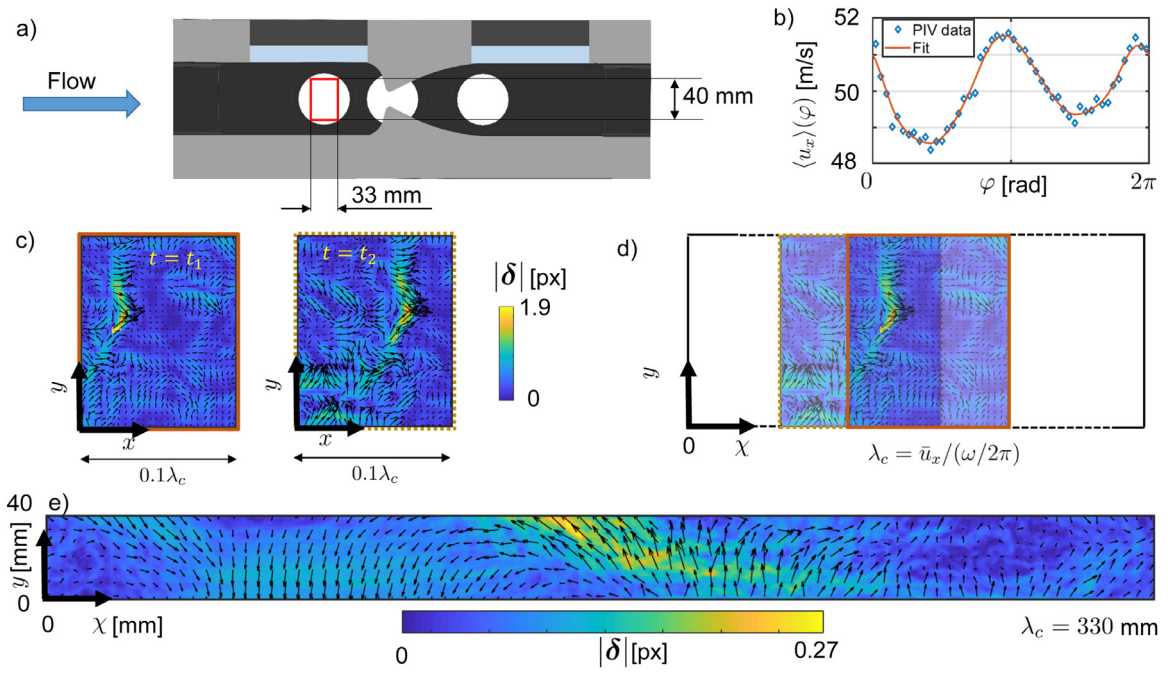

Fig. 4. a) Vertical cut through the nozzle section as shown in Fig. 1f. The red rectangle indicates the location of the FOV for BOS and PIV extraction for performing BOS thermometry. b) Example of phase averaged axial velocity from PIV (spatially averaged over the FOV) for pulsed-jet frequency of 145 Hz and jet temperature of 490 K. c) Individual BOS snapshots. d) Stitching process using PIV velocity. e) BOS displacement field representing an entire wavelength of the entropy wave. (For interpretation of the references to colour in this figure legend, the reader is referred to the web version of this article.)

the bulk flow velocity $\bar{u}_x(t)$. For that purpose, Particle Image Velocimetry (PIV) was conducted in the test section's vertical central plane. As depicted in Fig. 1(b), a high-speed camera (Photron SA-X2) was used to record Mie scattering images of theseeded flow illuminated by a laser light sheet at 5kHz. The light sheet was inserted through the top windows and the camera field of view (FOV) was adjusted to match the one of the second highspeed camera used for Background Oriented Schlieren (BOS). The focal plane of the PIV camera, which is inclined relative to the central plane of the test rig, was corrected using Scheimpflug optics. The camera was equipped with a Nikon AF 200 mm micro Nikkor lens and a 532 nm bandpassfilter from Edmund Optics. A Photonics DM60 Nd:YAG laser generated a pulsed 532 nm light sheet guided by a laser arm from Lavision to the sheet optics positioned above the test section.

The measurements of the line-of-sight (LOS) integrated refraction index gradient field $n(\boldsymbol{x}, t)$, perpendicular to the optical axis, are achieved via the quantification of the displacement field $\boldsymbol{\delta}(\boldsymbol{x}, t)$, by the Background Oriented Schlieren (BOS) setup, depicted in Fig. 1b. Its components are a highspeed camera (Photron SA-X2), equipped with a 200mm Nikon lens, pointing at the FOV shown by a red rectangle in Fig. 4(a), a water cooled transparent background and an illuminating LED (IL-106 from HardSoft). A thermostat was used to keep the background at ambient temperature. The scaling factors between the sensor, background plane and measurement plane were quantified using calibration targets. By taking the divergence on both sides of the classical BOS equation given in [47], we obtain the Poisson equation given below:

$$\nabla \cdot \nabla n(\boldsymbol{x}, t) = \frac{n_0}{W Z_d} \nabla \cdot \boldsymbol{\delta}(\boldsymbol{x}, t) \tag{4}$$

By solving Eq. (4), we determine the line of sight integrated refraction index field n. In this equation, $\boldsymbol{\delta}(\boldsymbol{x}, t)$ is the displacement vector field obtained by a cross-correlation algorithm between images of the illuminated background pattern. The thickness of the Schlieren object W is, in the present setup, the channel width in z-direction (see Fig. 1e), and Z_d is the distance from the channel center to the background plane (see Fig. 1(b)). The details of the procedure to obtain $\boldsymbol{\delta}(\boldsymbol{x}, t)$ are provided in [25].

These displacement fields are proportional to the instantaneous LOS-integrated refractive index gradients induced by the entropy waves passing the FOV. As indicated above, they are used to compute the coherent temperature fluctuations $\tilde{T}(\boldsymbol{x}, t)$, by integration of Eq. (4) and subsequent conversion. This integration cannot be performed directly, because of high axial mean flow velocities of around 50 m/s, only a fraction of the convective wavelength λ_c is captured in the individual snapshots $\boldsymbol{\delta}_e$. The method presented in [25] was developed to circumvent this problem. In short, the instantaneous displacement fields are stitched together as a function of the phase angle of the passing entropy wave, and afterward averaged before integrating the Poisson equation in order to obtain the coherent fluctuations of the refraction index $\tilde{n}$. This process is illustrated in Figs. 4c and 4d, and it necessitates the phase averaged mean axial velocity $\langle u_x \rangle(\varphi)$(see Fig. 4b) in order to position

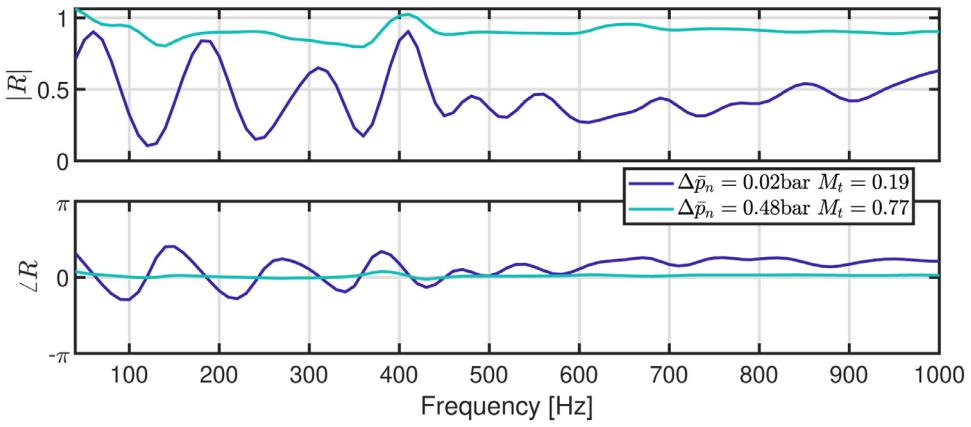

Fig. 5. Acoustic reflection coefficient obtained using the loudspeaker excitation for $M_t = 0.19$ and $M_t = 0.77$.

the images along a new axial coordinate $\chi(\varphi) = \omega^{-1} \int_0^{\varphi} \langle u_x \rangle(\phi) d\phi$, where φ is the instantaneous phase (modulo 2π) of the reconstructed acoustic pressure in the nozzle throat at the forcing frequency.

An example of coherent displacement field obtained with this method using 5000 instantaneous field recorded during 146 cycles is shown in Fig. 4e. The Gladstone-Dale relation and the ideals gas law are then used to deduce the coherent temperature fluctuations from the coherent fluctuations of the refraction index $\tilde{n}$ as explained in [25]. These LOS-integrated temperature fluctuations $\tilde{T}(\chi, y)$ will be presented in what follows by using the axial coordinate χ, which enables 2D spatial representation of the entropy waves at the FOV (just upstream of the nozzle), as if their amplitude decay had been frozen from this region. The entropy waves will also be averaged in the y direction in order to extract their amplitude and phase at the forcing frequency.

4. Results

4.1. Choked nozzle subject to incident acoustic waves

As a first step, the nozzle response to incident acoustic waves, in the absence of entropy waves, was measured. Using the loudspeaker as a sound source, the acoustic reflection coefficient was obtained over a wide frequency range, from 40 to 1000 Hz. Fig. 5(a) shows amplitude and phase of R for an increasing static pressure difference $\Delta \bar{p}_n$ across the nozzle and therefore also increasing Mach number M_t at the nozzle throat. Isentropic flow with a pressure ratio $\bar{p}/\bar{p}_0$ was assumed for the calculation of M_t[48]. The needed stagnation pressure $\bar{p}_0 = \bar{p} + \rho \bar{u}_x^2/2$ was obtained using measured values for the static pressure $\bar{p}$ and velocity values $\bar{u}_x$, that were calculated using the ideal gas law and the measured mass flow rate $\dot{m}_{tot} = \dot{m}_m + \dot{m}_j$. The modulus $|R|$ for the $M_t = 0.19$ in Fig. 5 displays several large peaks and valleys in the first half of the considered frequency range. For this low mass flow through the channel, the static pressure drop across the nozzle is not sufficient to decouple the acoustic field upstream of the nozzle from the one downstream. Consequently, there are ranges of frequencies for which the acoustic energy transmitted downstream of the nozzle can be stored into the resonances of the channel. For each of these longitudinal resonant modes, the downstream channel behaves as a bandpass filter for the acoustic energy transmission downstream of the nozzle. However, these resonances are significantly less pronounced beyond the cut-off frequency set by the horn and the acoustic foam lining in the downstream plenum (see Fig. 1(a)). Indeed, beyond that cut-off frequency (at about 500 Hz), a significant part of the acoustic energy of the downstream travelling acoustic waves is transmitted by the horn and absorbed by the foam, while only a small fraction of it is reflected, which prevents the establishement of strong resonances in the downstream channel beyond that frequency.

As M_t increases, $|R|$ approaches 1, which is consistent with the classic theoretical predictions [26]. The sonic flow in the nozzle acoustically decouples the upstream channel from the downstream one. The phase is going towards 0, which is expected, since the upstream side of a choked nozzle behaves acoustically like a hard wall.

The decay of entropy waves rapidly increases with the Strouhal number $St = \omega L/(2\pi U)$, which is defined by the combustion chamber length L and the mean flow velocity U. Consequently, the participation of entropy waves to thermoacoustic instabilities is limited to low-frequency constructive feedback loops. The instabilities which occur at very low frequency are the so-called rumble instabilities. Indeed, the frequency of rumble is defined by the long convection time from the flame to the combustor exit, and it can be significantly lower than the frequency of the first acoustic eigenmode of the combustor [5]. In [25], which considers the same test rig as in the present work, but without nozzle and at different mass flows, it was shown that for downstream location corresponding to $St > 3$, entropy wave amplitudes decay by at least a factor of ten. Assuming i) that the combustion chamber of a large land-based gas-turbine combustion chamber exhibit similar wave dispersion as in [25], and ii) that it has a length $L = 1$m, a hot gas velocity $U = 50$m/s and coherent temperature fluctuations

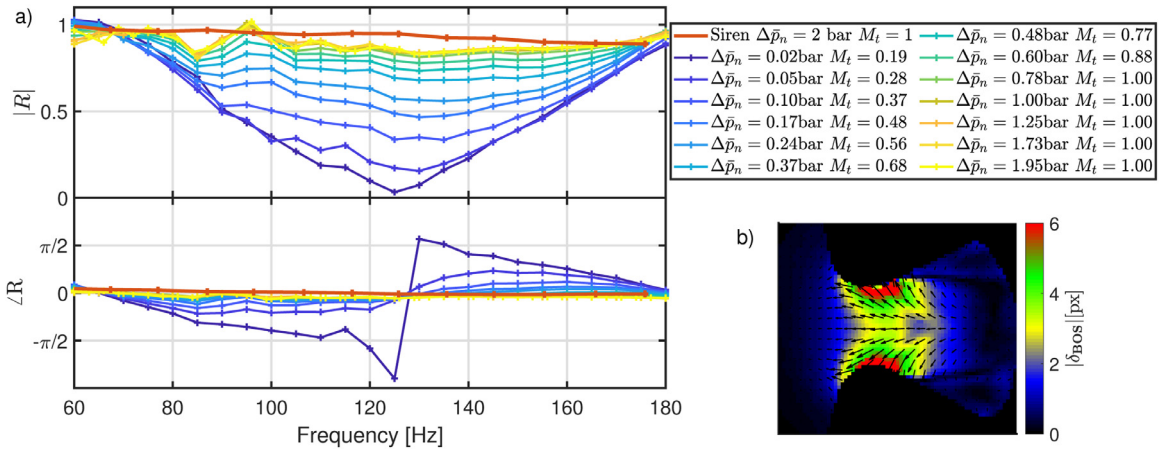

Fig. 6. a) Reflection coefficient measurement for increasing pressure drop across the nozzle without entropy wave. b) BOS displacement field induced by the presence of a shock cell downstream of the nozzle throat, for $\Delta p_n = 2$ bar.

of amplitude $|\tilde{T}|/\bar{T} = 0.1$ at the beginning of the chamber (where the flame is located), then, the entropy wave amplitude at the turbine inlet will have decayed below 1% of the mean temperature for frequencies greater than 150 Hz. Note that such 'back of the envelope' calculation is not robust because the dispersion will be highly dependant on the type of burner and on the combustor dispersion as shown in [11]. In the present work, the frequency range from 60 to 180 Hz was selected for the analysis of the production of sound by entropy waves passing through the choked nozzle. This range is relevant for combustors of large gas turbines. It is possibly too low for aero-engine applications, which exhibit shorter chambers. Besides, it corresponds to *St* between 0.6 and 1.8, for which entropy wave amplitudes at the nozzle are between 75% and 25% of their initial value at the siren in the present configuration [25].

In Fig. 6, the measurement of the reflection of pure acoustic waves using the loudspeaker forcing was refined in that frequency range for a series of M_t. Then, the reflection coefficient of acoustic waves without entropy waves was also performed using the siren for $M_t = 1$(red curve). For that measurement, the siren heater was adjusted to deliver a pulsed jet at the same temperature $\bar{T}_j$ as the one of the main flow $\bar{T}_m = 43°$C, such that no entropy-waves-induced backward acoustic waves were produced. The acoustic forcing generated by the siren was roughly one order of magnitude higher than the one of the speaker excitation, reaching a maximum amplitude of 50 mbar for some excitation frequencies. As expected, the obtained reflection coefficients closely align with the loudspeaker results for both amplitude and phase. In what follows, this reflection coefficient measurement serves as reference R_{ref} to quantify the entropy-wave-induced reflected acoustic wave for the cases with $\bar{T}_j \neq \bar{T}_m$. All further measurements were performed at $\Delta\bar{p}_n = 2$ bar, $\bar{p} = 3$ bar and $M_t = 1$, for which a significant entropy response is expected.

Fig. 6b shows the absolute values of the displacement field obtained at the nozzle by applying the classical BOS correlation method [49]. The large displacements in the throat area are due to the presence of a shock cell. The interested reader can refer to [50] for a recent work on the application of BOS for three-dimensional density field reconstruction of underexpanded jets.

4.2. Entropy-wave-induced backward acoustic waves

To produce entropy-wave-induced sound, the jet temperature $\bar{T}_j$ was adjusted to higher or lower values than the main flow temperature $\bar{T}_m = 43$ °C. For qualitative observation of entropy waves when they reach the nozzle, oil droplets of a few mdiameter were injected in the main flow, but not in the siren flow for the pulsed jet, taking advantage of the incomplete mixing at the nozzle for the range of Strouhal numbers considered here (from $St = 0.6$ at 60 Hz to $St = 1.8$ at 180 Hz, with a mean flow velocity of about 50 m/s and a distance from the jet to the nozzle of 0.49 m). By illuminating these droplets with the laser sheet, the seeding density differences become observable using the PIV high-speed camera, with the FOV on the nozzle throat (middle sapphire window in Fig. 1(f)).

A set of consecutive raw images of the Mie scattering is presented in Fig. 7a. One can visualize the change of light intensity associated with the passage of an entropy wave. Due to limited optical access from the top, it was not possible to illuminate the entire channel height at the throat. The Mie scattering intensity integrated over the region, delimited by the red rectangle in Fig. 7(a), is shown in the top row of Fig. 7(b). The signal shows clear oscillation at the pulsed-jet frequency of 145 Hz, as shown in Fig. 7(c). This Mie scattering intensity can be used to determine the phase difference between the incident entropy waves and the incident acoustic wave at the nozzle throat. The Fourier coefficient at the fundamental frequency $\omega/2\pi$ was extracted and plotted in the middle row of Fig. 7 b. Since the siren flow is not seeded, the coherent Mie scattering signal $\tilde{I}_{\text{Mie}}$ is minimal when $\tilde{T}$ is at its maximum for $\bar{T}_j > \bar{T}_m$ or when $\tilde{T}$ is at its minimum when

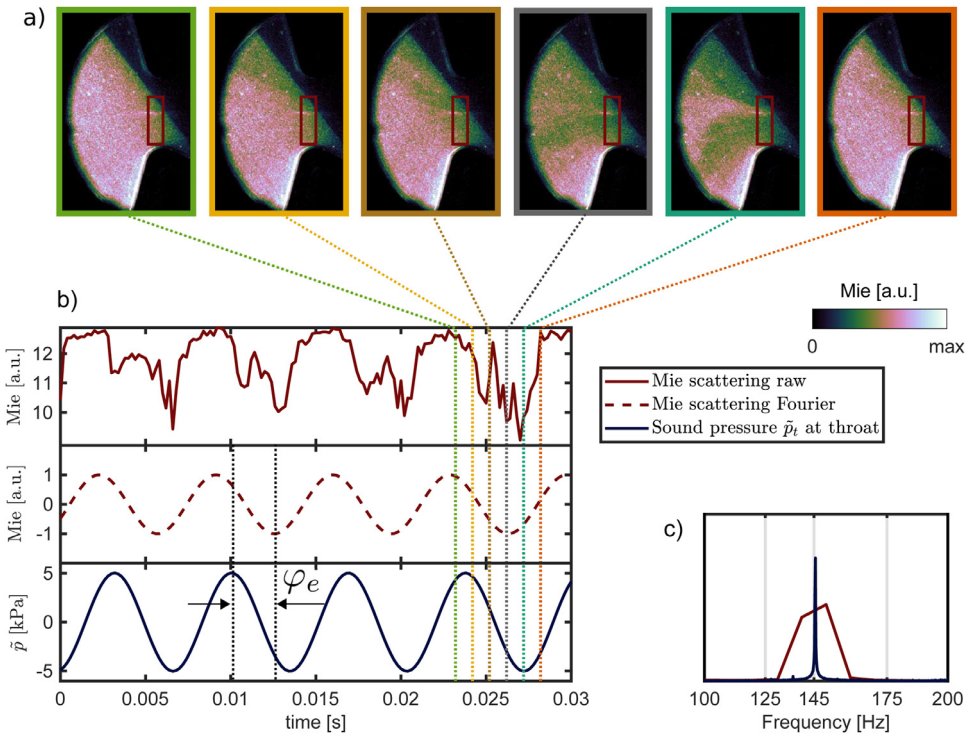

Fig. 7. a) Raw, instantaneous Mie scattering signal (a movie is available in the supplementary material). b) Top: Spatially-integrated instantaneous Mie scattering signal in the red box shown in a). Middle: Extracted coherent part of the instantaneous Mie scattering signal. Bottom: Reconstructed acoustic pressure at the nozzle throat, with φ_e being the phase difference between entropy waves and reflected acoustic waves. c) Spectra of the Mie scattering signal and of the acoustic pressure shown in b). (For interpretation of the references to colour in this figure legend, the reader is referred to the web version of this article.)

$\bar{T}_j < \bar{T}_m$. The bottom row in Fig. 7(b) shows the acoustic pressure at the nozzle throat $\tilde{p}_t$ reconstructed from the multi-microphone method. The phase difference $\varphi_e = \angle\tilde{p}_t - \angle\tilde{I}_{\text{Mie}} + \pi$, between $\tilde{p}_t$ peaks and $\tilde{I}_{\text{Mie}}$ valleys, therefore represents the phasing between the acoustic pressure fluctuations and entropy waves at the nozzle. For the extraction of this averaged phase difference between acoustic and entropy waves, time traces of 16 cycles were used. This interval corresponds to a train of entropy spots produced during one full rotation of the siren disk, which exhibits 16 equally-spaced holes. This procedure led to relative errors between the extracted and reconstructed acoustic pressure amplitudes below 5% for all the piezo sensors. The reflection coefficients obtained at different $\Delta T_{jm} = \bar{T}_j - \bar{T}_m$ are plotted in Fig. 8a and b. The purely acoustic case with $\Delta T_{jm} \approx 0$ serves as reference R_{ref}. Between 80 and 120 Hz, $|R|$ is larger than $|R_{\text{ref}}|$ for accelerated cold waves, while above 130 Hz, $|R|$ is larger than $|R_{\text{ref}}|$ if hot waves are impinging on the nozzle. For the hot cases, data was recorded for two intermediate ΔT_{jm} values, for which $|R|$ and $\angle R$ are in a consistent trend with the other measurements.

The observed differences in $|R|$ originate from the sound produced by the acceleration of the temperature waves in the nozzle, which is superimposed to the reflected sound. The Riemann invariant g, defining the upstream-travelling acoustic wave is affected by the constructive or destructive interference of the two components of the backward acoustic waves. The phasing between them depends on the frequency, because the downstream travelling wave with complex amplitude f propagates at $\bar{u}_x + \bar{c}$ while the entropy waves are advected at about $\bar{u}_x$, where c is the local speed of sound and u_x the bulk flow velocity in the axial direction. As one can see in Fig. 8, the measurements indicate that entropy waves with negative fluctuations of the temperature produce acoustic pressure fluctuations having an opposite sign compared to the ones produced by positive temperature fluctuations.

The circles in Fig. 8 correspond to the reflection coefficients measured during the experiments with the particle seeding for PIV and Mie scattering imaging. They were measured on a different date and are in close agreement with ones measured without particle seeding. Both absolute value and phase angle match closely in almost all cases. The seeding therefore has negligible effects on the acoustic end result.

The diamonds in Fig. 8 show φ_e, obtained from the experiments with seeding on. For the pulsed jet frequency set to 145 Hz, φ_e is distributed in the vicinity of π for the five ΔT_{jm} cases. At this frequency, $|R|$ is higher than the $|R_{\text{ref}}|$ for the entropy wave induced by the periodic acceleration of hot spots in the nozzle and the highest $|R|$, obtained for the highest positive temperature fluctuations, clearly exceeds 1, which can have important consequences on the thermoacoustic stability of a combustor. From the literature, e.g. [26,43], it is known that accelerated hot spots result in negative pressure pulses. To constructively interact, the hot waves therefore need to be out of phase by $\varphi_e = \pi$, which is in agreement with the present

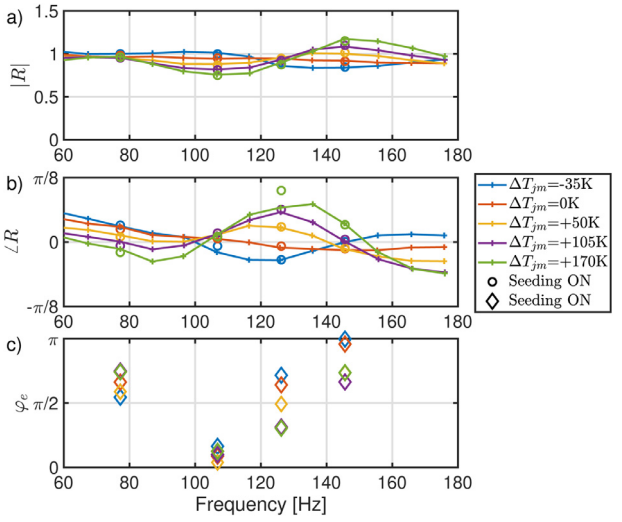

Fig. 8. a) Modulus of the measured reflection coefficients R for different siren temperature settings. Some of the points were repeated on a different day with seeding on (circles). b) Phase of R. c) φ_e, obtained by Mie scattering analysis. The color code of the circles and diamonds depends on applied ΔT_{jm} and matches the color code of the unseeded experiments.

findings that $|R|$ is maximized around this frequency for the hot waves. The spread of the estimated φ_e at the different frequencies can be primarily explained by the fact that ΔT_{jm} influences the momentum of the pulsed-jet and its penetration in the cross flow, and hence has an influence on the effective average propagation speed $\bar{u}_x$ and consequently on φ_e. This is in line with the ordering of the estimated φ_e, with points that shift slightly with changing mean flow temperature. In addition, the Mie scattering information is obtained in the central plane which does not quantify possible coherent deformation of the hot and cold spots in the line-of-sight direction.

Following the same reasoning, at the excitation frequency of 116 Hz, the entropy waves are in phase with the acoustics ($\varphi_e \approx 0$) and one can explain the evolution of the measured reflection coefficient when ΔT_{jm} is changed: The acoustic waves produced by the acceleration of hot spots interfere destructively with the ones produced from the reflection of incident acoustic waves, resulting in $|R| < |R_{\text{ref}}|$. The acceleration of cold spots however, leads to a constructive interference, which leads to the conclusion that cold spots indeed cause positive pressure peaks when they are accelerated in the sonic nozzle. Finally, for the excitation frequencies of 76 Hz and 126 Hz, $\varphi_e \simeq \pi/2$ and $|R| \simeq |R_{\text{ref}}|$, which means the presence of entropy-wave induced sound does not affect the magnitude of the backward acoustic waves but primarily their phase.

4.3. BOS thermometry results

To enable quantitative measurements of the conversion of temperature waves into sound waves, the coherent wave amplitude $\tilde{T}$ at the nozzle has to be known. The measurement of ΔT_{jm} at the siren injection is not sufficient, because the temperature of the periodic hot spots decays toward the mean flow temperature due to shear dispersion during advection toward the nozzle. Therefore, BOS thermometry was performed close to the nozzle inlet. Because the method requires intense post-processing and is quite data intensive, it was only applied for nine different ΔT_{jm} at the pulsed-jet frequency of 145 Hz, which is the frequency at which the strongest constructive effect in term of reflection coefficient magnitude was observed, as shown in Fig. 8. Fig. 9 shows the obtained 2D line-of-sight integrated $\tilde{T}$ distributions. ΔT_{jm} is gradually increased from top to bottom. The colored diamonds on the left indicate the corresponding ΔT_{jm} value, following the same color code as Fig. 10. In the top field, the cold wave is visible in the center. The temperature of this central region, gradually increases to the bottom field, where the largest ΔT_{jm} was applied. The reconstructed temperature distributions are not perfectly homogeneous in the vertical direction, which is also in-line with the Mie scattering images in Fig. 7a. It means that the pulsed-jet-in-cross-flow is not strong enough to reach the bottom of the channel. This also explains that the maximum amplitude values are measured in the upper half of the channel, because this is where they were injected upstream.

The reference case $\Delta T_{jm} = 0.18$K shows a non-zero amplitude. This arises from the difficulty of perfectly tuning the siren heater to match $\bar{T}_j$ and $\bar{T}_m$. Indeed, the heater was manually tuned such that the thermocouple placed just downstream of the heater inside the siren matched the temperature of the steady state main flow, measured by a thermocouple 40 cm upstream of the pulsed jet of the siren. The channel walls guiding the main flow are not isolated, which leads to slight heat losses that reduce the main flow temperature which therefore is slightly lower than $\bar{T}_j$, resulting in non-zero $\tilde{T}$. The length of the obtained temperature fields is equal to the convective wave length λ_c, and therefore is slightly larger for the hotter cases, as the advection speed u_x increases with temperature.

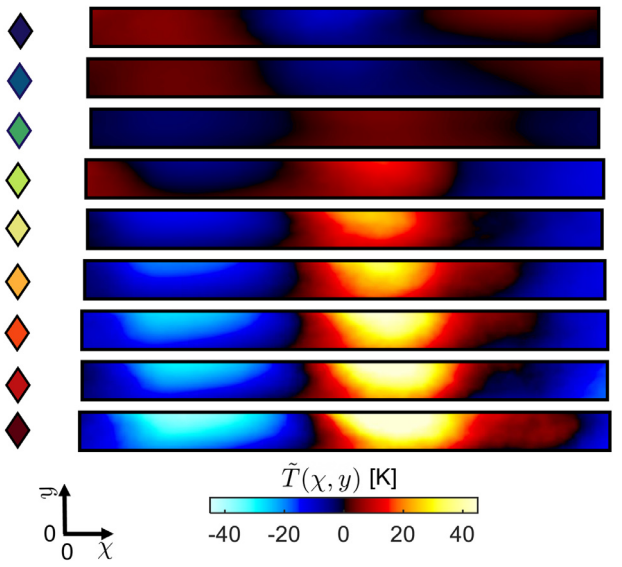

Fig. 9. Reconstructed $\tilde{T}(\chi, y)$ fields for the advection of periodic cold and hot spots at a frequency of 145 Hz and at the position indicated by the red rectangle in Fig. 4a. As explained in the text, the axial coordinate χ allows a spatial representation of the entropy wave along a full convective wavelength of about $2\pi\bar{u}_x/\omega \approx 50/145 = 345$mm, as if its decay had been frozen from the measurement location (red rectangle, whose length is 33 mm). The color code of diamonds matches the code used in Fig. 10. (For interpretation of the references to colour in this figure legend, the reader is referred to the web version of this article.)

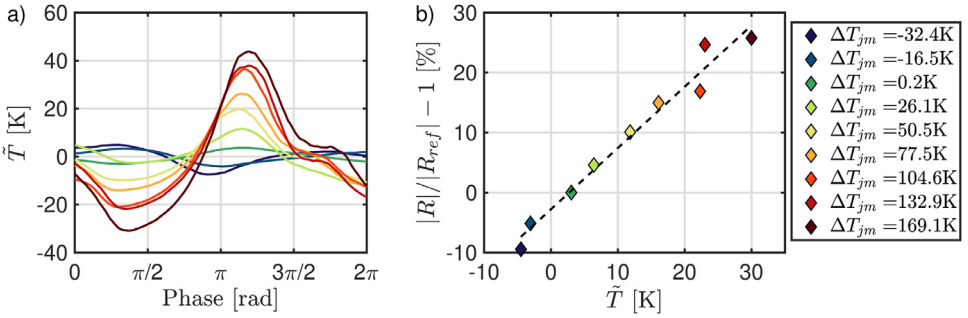

Fig. 10. a) Measured coherent temperature fluctuations averaged along the y coordinate. b) Extracted Fourier amplitudes at the fundamental excitation frequency of 145 Hz versus the relative change of $|R|$.

For further analysis, the $\tilde{T}(\chi, y)$ fields were averaged over the channel cross section, leading to the $\tilde{T}$, shown in Fig. 10 a. Also here, the increase of ΔT_{jm} leads to a consistent increase in amplitude of $\tilde{T}$. The shape of these curves is caused by the dynamics of the injection process. Since only the coherent component is relevant for the production of sound at the pulsed jet frequency, the Fourier coefficient at this frequency was extracted for each measurement and plotted against $|R|/|R_{\text{ref}}| - 1$ in Fig. 10(b). For $\bar{T}_j \neq \bar{T}_m$, the measured reflection coefficient varied by up to 30% with respect to $|R_{\text{ref}}|$. This difference was found to be directly proportional to $\tilde{T}$ in the measured range. This is an expected result and also confirms the previous findings that the acceleration of cold spots lead to opposite sign effects. This linear relation is shown by a dashed line in Fig. 10(b). The fact that it does not cross the origin is explained by the non perfect reference. With this experimental platform and the employed techniques, the achievement here is a direct quantification of the relationship between the acoustic waves reflected by a nozzle subject to the incidence of combined acoustic and entropy waves at a relatively high frequency in a highly turbulent flow upstream of the nozzle.

4.4. Separation of acoustic and entropy-wave induced reflected-sound

The measured upstream travelling wave $g = g_a + g_e$ contains both the reflected acoustics g_a and the entropy wave contribution g_e resulting from the conversion of the hot/cold spots acceleration in the nozzle throat into acoustic waves. As it was done in previous work, e.g. [34], the reflection coefficient R can be decomposed into a purely acoustic part $R_a = g_a/f$, quantifying the reflection of incident acoustic waves f, and an entropy-wave related reflection coefficient $R_e = (g_e/c)/(\tilde{T}/\bar{T})$ characterizing the conversion of accelerated entropy waves into g_e. In a matrix form, the net upstream travelling wave g can

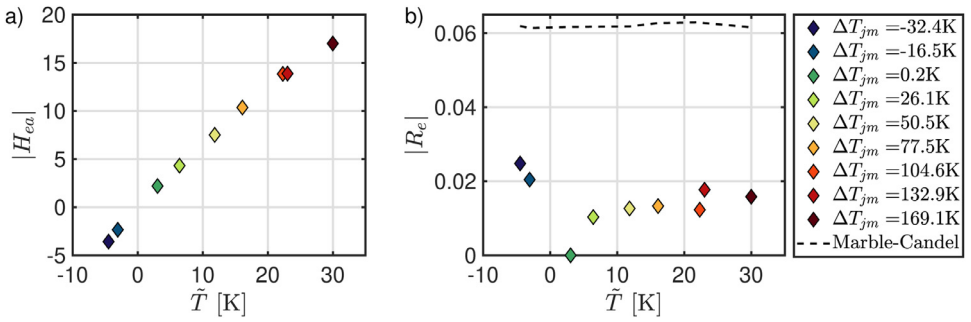

Fig. 11. a) The relative entropy forcing strength H_{ea} as a function of the measured temperature amplitude $\tilde{T}$. b) The modulus of R_e plotted as a function of $\tilde{T}$ and compared to the theoretical result from [26] for a compact sonic nozzle. All measurements were obtained at a frequency of 145 Hz.

be written as:

$$\frac{g}{c} = \begin{pmatrix} \frac{f}{c} & \frac{\tilde{T}}{\bar{T}} \end{pmatrix} \begin{pmatrix} R_a \\ R_e \end{pmatrix} = \frac{f}{c} \overbrace{\left(R_a + \frac{\tilde{T}/\bar{T}}{f/c} R_e\right)}^{R} \tag{5}$$

The experimentally measured total reflection coefficient R relates the forward and backward acoustic waves g and f. Defining the relative entropy-wave forcing strength $H_{ea} = (\tilde{T}/\bar{T})/(f/c)$, one can write:

$$R = R_a + H_{ea} R_e \tag{6}$$

By measuring the amplitude of $\tilde{T}$ with BOS thermometry and determining the corresponding phase φ_e by Mie scattering wave tracking, the complex H_{ea} is quantified. The entropy-wave-to-acoustic-wave conversion coefficient $R_e = (R - R_a)/H_{ea}$ can then be deduced by using the measured acoustic reflection coefficient in absence of incident entropy waves (for which $R_e = 0$ since $R = R_a = R_{\text{ref}}$):

$$R_e = \frac{R - R_{\text{ref}}}{H_{ea}} \tag{7}$$

In [26], Marble & Candel derived an analytical expression for R_e in supercritical compact nozzle flows, that depends only on the upstream Mach number M_u:

$$R_e = -\frac{\frac{1}{2} M_u}{1 + \frac{1}{2}(\gamma - 1) M_u} \tag{8}$$

In Fig. 11(b), the results of this model at $M_u \approx 0.143$ are compared to the experimental values, whose gain magnitudes are around 60% lower than the model prediction.

The lower gain can be explained by the following reasons: First, the measurement of the entropy wave amplitude is performed a short distance upstream of the nozzle (see red rectangle in Fig. 4) and its amplitude will further decay along the last few centimeters to the nozzle. Second, the entropy perturbations occur via highly three dimensional (3D) structures in the turbulent flow field, and during their acceleration, these hot or cold pockets are subject to 3D deformation, which is clearly visible in the Mie scattering images presented in Fig. 7(a). This 3D nature of the hot or cold pockets enhances their dispersion and mixing with the main stream. These resulting elongated temperature streaks lead to a reduction of the effective temperature fluctuation amplitude in the nozzle [36], which reduces the resulting sound amplitude. Additionally, the BOS temperature fields and Mie Scattering images, make it clear that the vertical temperature distribution within the temperature waves was not symmetrical, because the pulsed jet-in-crossflow did not penetrate enough. The higher amplitude in the top half of the channel probably also contributed significantly to the reduction in entropic sound generated, compared to the 1D result of Marble & Candel. It therefore calls for further research, both in terms of experiments and in terms of model development. For instance, such experimental setup could also be used to quantify the sound waves produced by pure coherent compositional waves [2], by generating with the siren a pulsed jet of heavier or lighter gases into the air crossflow while keeping the two stream at the same temperature. Following up on the recent studies [36,37], it would also be interesting to simulate the acceleration of turbulent hot spots in a practical turbine inlet geometry, and then relate the turbulent properties of the periodic hot spots to the sound that they generate.

5. Conclusion

The contribution of backward acoustic waves produced by the acceleration of coherent temperature fluctuations into a choked nozzle on the sound field upstream of this nozzle has been quantified experimentally. The flow upstream of the nozzle was highly turbulent, shock cells were identified in the nozzle and the entropy waves in the upstream flow were

generated between 60 and 180 Hz using a pulsed jet in the main cross flow, whose temperature was controlled using an electric heater or a cold heat exchanger. The mass flow added by this pulsed jet was approximately eight percent of the one of the main flow supplied from a compressor. Coherent temperature fluctuations arriving at the nozzle and flow velocity were respectively measured using BOS thermometry and PIV. The forward and backward acoustic waves were measured using the multi-microphone method. Moreover, the constructive or destructive interference between entropy-wave induced backward acoustic waves and backward acoustic wave resulting from the reflection of the forward ones was scrutinized and explained. This information was also used to quantify, from 60 to 180 Hz, the relationship between the incident entropy waves and the resulting backward travelling acoustic wave. This indirect sound production was approximately 60% lower than the result predicted by the classic one dimensional model of Marble & Candel for supercritical compact nozzles. Based on the Mie scattering images of the seeded flow at the nozzle and on the BOS thermometry results, it is concluded that this difference is likely due to the three dimensional deformation of coherent entropy spots during their acceleration in the nozzle as well as because the entropy spots do not span over the entire cross-section of the channel, which leads to lower effective temperature fluctuation amplitudes in the nozzle throat. This work encourages further experimental and modelling research for predicting the contribution of entropy waves on thermoacoustic instabilities in real turbulent combustors.

Declaration of Competing Interest

The authors declare that they have no known competing financial interests or personal relationships that could have appeared to influence the work reported in this paper.

Supplementary material

Supplementary material associated with this article can be found, in the online version, at doi:10.1016/j.jsv.2020.115799.

CRediT authorship contribution statement

Markus Weilenmann: Investigation, Methodology, Visualization, Writing - original draft. **Nicolas Noiray:** Conceptualization, Supervision, Methodology, Writing - original draft.

References

[1] C.K. Tam, S.A. Parrish, The physical processes of indirect combustion noise generation, International Journal of Aeroacoustics 17 (1–2) (2018) 22–35.
[2] L. Magri, J. O'Brien, M. Ihme, Compositional inhomogeneities as a source of indirect combustion noise, J Fluid Mech 799 (2016), doi:10.1017/jfm.2016.397.
[3] S.R. Stow, A.P. Dowling, T.P. Hynes, Reflection of circumferential modes in a choked nozzle, J Fluid Mech 467 (2002) 215–239, doi:10.1017/S0022112002001428.
[4] I. Duran, S. Moreau, F. Nicoud, L. T., E. Bouty, T. Poinsot, Combustion noise in modern aero-engines, AerospaceLab 7 (2014) 1–11, doi:10.12762/2014.AL07-05.
[5] A.P. Dowling, Y. Mahmoudi, Combustion noise, Proc. Combust. Inst. 35 (1) (2015) 65–100.
[6] A.S. Morgans, I. Duran, Entropy noise: a review of theory, progress and challenges, International Journal of Spray and Combustion Dynamics 8 (4) (2016) 285–298.
[7] T. Poinsot, Prediction and control of combustion instabilities in real engines, Proc. Combust. Inst. 36 (1) (2017) 1–28.
[8] W. Polifke, C.O. Paschereit, K. Döbbeling, Constructive and destructive interference of acoustic and entropy waves in a premixed combustor with a choked exit, International Journal of Acoustics and Vibration 6 (3) (2001) 135–146.
[9] R. Bluemner, C.O. Paschereit, K. Oberleithner, Generation and transport of equivalence ratio fluctuations in an acoustically forced swirl burner, Combust Flame 209 (2019) 99–116.
[10] T. Sattelmayer, Influence of the combustor aerodynamics on combustion instabilities from equivalence ratio fluctuations, Journal of Engineering for Gas Turbine and Power 125 (1) (2002) 11–19.
[11] M. Weilenmann, U. Doll, R. Bombach, A. Blond, D. Ebi, Y. Xiong, N. Noiray, Linear and nonlinear entropy-wave response of technically-premixed jet-flames-array and swirled flame to acoustic forcing, in: Proceedings of the Combustion Institute, 2020. Doi:10.1016/j.proci.2020.06.233
[12] J. Eckstein, T. Sattelmayer, Low-order modeling of low-frequency combustion instabilities in aeroengines, J. Propul. Power 22 (2) (2006) 425–432, doi:10.2514/1.15757.
[13] G. Wang, X. Liu, S. Wang, L. Li, F. Qi, Experimental investigation of entropy waves generated from acoustically excited premixed swirling flame, Combust Flame 204 (2019) 85–102.
[14] B. Semlitsch, T. Hynes, I. Langella, N. Swaminathan, A.P. Dowling, Entropy and vorticity wave generation in realistic gas turbine combustors, J. Propul. Power 35 (4) (2019) 839–849.
[15] T. Steinbacher, M. Meindl, W. Polifke, Modelling the generation of temperature inhomogeneities by a premixed flame, International Journal of Spray and Combustion Dynamics 10 (2) (2018) 111–130.
[16] L.S. Chen, S. Bomberg, W. Polifke, Propagation and generation of acoustic and entropy waves across a moving flame front, Combust Flame 166 (2016) 170–180.
[17] A.S. Morgans, C.S. Goh, J.A. Dahan, The dissipation and shear dispersion of entropy waves in combustor thermoacoustics, J Fluid Mech 733 (2013).
[18] A. Fattahi, S.M. Hosseinalipour, N. Karimi, On the dissipation and dispersion of entropy waves in heat transferring channel flows, Physics of Fluids 29 (8) (2017) 087104.
[19] L. Christodoulou, N. Karimi, A. Cammarano, M. Paul, S. Navarro-Martinez, State prediction of an entropy wave advecting through a turbulent channel flow, J Fluid Mech 882 (2020) A8.
[20] J. Rodrigues, A. Busseti, S. Hochgreb, Numerical investigation on the generation, mixing and convection of entropic and compositional waves in a flow duct, J Sound Vib 472 (2020) 115155, doi:10.1016/j.jsv.2019.115155.
[21] Y. Mahmoudi, A. Giusti, E. Mastorakos, A.P. Dowling, Low-Order modeling of combustion noise in an aero-engine: the effect of entropy dispersion, J Eng Gas Turbine Power 140 (1) (2017).
[22] Y. Xia, I. Duran, A.S. Morgans, X. Han, Dispersion of entropy perturbations transporting through an industrial gas turbine combustor, Flow Turbulence and Combustion 100 (2) (2018) 481–502.

[23] W. Polifke, Modeling and analysis of premixed flame dynamics by means of distributed time delays, Prog Energy Combust Sci 79 (2020) 100845.
[24] A. Giusti, N.A. Worth, E. Mastorakos, A.P. Dowling, Experimental and numerical investigation into the propagation of entropy waves, AIAA Journal 55 (2) (2017) 446–458.
[25] M. Weilenmann, Y. Xiong, N. Noiray, On the dispersion of entropy waves in turbulent flows, J Fluid Mech 903 (2020) R1, doi:10.1017/jfm.2020.703.
[26] F. Marble, S. Candel, Acoustic disturbance from gas non-uniformities convected through a nozzle, J Sound Vib 55 (2) (1977) 225–243.
[27] M. Huet, A. Giauque, A nonlinear model for indirect combustion noise through a compact nozzle, J Fluid Mech 733 (2013) 268–301, doi:10.1017/jfm.2013.442.
[28] M. Huet, Nonlinear indirect combustion noise for compact supercritical nozzle flows, J Sound Vib 374 (2016) 211–227, doi:10.1016/j.jsv.2016.03.028.
[29] C.S. Goh, A.S. Morgans, Phase prediction of the response of choked nozzles to entropy and acoustic disturbances, J Sound Vib 330 (21) (2011) 5184–5198, doi:10.1016/j.jsv.2011.05.016.
[30] W.H. Moase, M.J. Brear, C. Manzie, The forced response of choked nozzles and supersonic diffusers, J Fluid Mech 585 (2007) 281–304, doi:10.1017/S0022112007006647.
[31] I. Duran, S. Moreau, Solution of the quasi-one-dimensional linearized euler equations using flow invariants and the magnus expansion, J Fluid Mech 723 (2013) 190–231, doi:10.1017/jfm.2013.118.
[32] A. Giauque, M. Huet, F. Clero, Analytical analysis of indirect combustion noise in subcritical nozzles, Journal of Engineering for Gas Turbines and Power 134 (11) (2012), doi:10.1115/1.4007318. 111202
[33] E.O. Rolland, F. De Domenico, S. Hochgreb, Theory and application of reverberated direct and indirect noise, J Fluid Mech 819 (2017) 435–464, doi:10.1017/jfm.2017.183.
[34] F.D. Domenico, E.O. Rolland, S. Hochgreb, A generalised model for acoustic and entropic transfer function of nozzles with losses, J Sound Vib 440 (2019) 212–230.
[35] A. Ceci, R. Gojon, M. Mihaescu, Large eddy simulations for indirect combustion noise assessment in a nozzle guide vane passage, Flow, Turbulence and Combustion 102 (2) (2019) 299–311, doi:10.1007/s10494-018-9964-9.
[36] A. Emmanuelli, J. Zheng, M. Huet, A. Giauque, T. Le Garrec, S. Ducruix, Description and application of a 2D-axisymmetric model for entropy noise in nozzle flows, J Sound Vib 472 (2020) 115163, doi:10.1016/j.jsv.2019.115163.
[37] M. Huet, A. Emmanuelli, T. Le Garrec, Entropy noise modelling in 2D choked nozzle flows, J Sound Vib 488 (2020) 115637, doi:10.1016/j.jsv.2020.115637.
[38] F. Bake, C. Richter, B. Mhlbauer, N. Kings, I. Rhle, F. Thiele, B. Noll, The entropy wave generator (EWG): a reference case on entropy noise, J Sound Vib 326 (3) (2009) 574–598.
[39] S. Moreau, C. Becerril, L. Gicquel, Large-eddy-simulation prediction of indirect combustion noise in the entropy wave generator experiment, International Journal of Spray and Combustion Dynamics 10 (2) (2018) 154–168, doi:10.1177/1756827717740775.
[40] I. Durn, S. Moreau, T. Poinsot, Analytical and numerical study of combustion noise through a subsonic nozzle, AIAA Journal 51 (1) (2013) 42–52, doi:10.2514/1.J051528.
[41] M. Leyko, S. Moreau, F. Nicoud, T. Poinsot, Numerical and analytical modelling of entropy noise in a supersonic nozzle with a shock, J Sound Vib 330 (16) (2011) 3944–3958, doi:10.1016/j.jsv.2011.01.025.
[42] J.-M. Lourier, A. Huber, B. Noll, M. Aigner, Numerical analysis of indirect combustion noise generation within a subsonic nozzle, AIAA Journal 52 (10) (2014) 2114–2126, doi:10.2514/1.J052755.
[43] F.D. Domenico, E.O. Rolland, S. Hochgreb, Detection of direct and indirect noise generated by synthetic hot spots in a duct, J Sound Vib 394 (2017) 220–236.
[44] W. Tao, T. Schuller, M. Huet, F. Richecoeur, Coherent entropy induced and acoustic noise separation in compact nozzles, J Sound Vib 394 (2017) 237–255, doi:10.1016/j.jsv.2017.01.012.
[45] B. Schuermans, V. Bellucci, F. Guethe, F. Meili, P. Flohr, C.O. Paschereit, A detailed analysis of thermoacoustic interaction mechanisms in a turbulent premixed flame, Proceedings of the ASME Turbo Expo (2004) 539–551, doi:10.1115/GT2004-53831.
[46] H. Bodn, M. bom, Influence of errors on the two-microphone method for measuring acoustic properties in ducts, J. Acoust. Soc. Am. 79 (2) (1986) 541–549.
[47] M. Raffel, H. Richard, G.E.A. Meier, On the applicability of background oriented optical tomography for large scale aerodynamic investigations, Exp Fluids 28 (5) (2000) 477–481.
[48] J.D. Anderson, Fundamentals of Aerodynamics, McGraw (2009).
[49] M. Raffel, Background-oriented schlieren (BOS) techniques, Exp Fluids 56 (3) (2015) 60.
[50] F. Nicolas, D. Donjat, O. Lon, G. Le Besnerais, F. Champagnat, F. Micheli, 3D reconstruction of a compressible flow by synchronized multi-camera bos, Exp Fluids 58 (5) (2017).